Combining 77–81 GHz MIMO FMCW radar with frequency-steered antennas: a case study for 3D target localization

Patrick Kwiatkowski [ID], Alexander Orth [ID] and Nils Pohl [ID]

Institute of Integrated Systems, Ruhr University Bochum, Bochum, Germany

Abstract

In this paper, we introduce a compact 6×8 channel multiple-input multiple-output frequency-modulated continuous-wave radar system capable of determining the three-dimensional positions of targets despite utilizing a linear virtual array. The compact system, containing two cascaded radar transceiver ICs, has 48 virtual channels. We conduct a direction of arrival estimation with these virtual channels to determine the azimuth angle. To overcome the spatial limitation of the linear array, we use frequency-steered transmit antennas, which vary their main lobe direction during the frequency chirp, allowing the elevation angle to be determined by using a sliding window fast Fourier transform algorithm. In this study, we present the system's concept along with the associated signal processing. By taking measurements in different scenarios, each with differently placed corner reflectors, we investigate the capability of the system to separate adjacent targets concerning range, azimuth, and elevation. These measurements are additionally employed to point out the design trade-offs inherent to the system.

Introduction

In comparison to conventional phased array radar systems, multiple-input multiple-output (MIMO) radar systems provide the advantage of target localization with comparable angular resolution while using fewer antenna elements. This leads to lower hardware complexity due to a reduction in the number of channels, but at the same time provides for increased computational effort in signal processing. The ability to separate targets in three dimensions depends on range resolution and angular resolution in both azimuth and elevation. While range resolution mainly depends on the radar bandwidth, the angular resolution is primarily determined by the number and the arrangement of the transmit (TX) and receive (RX) antenna elements. Several MIMO frequency-modulated continuous-wave (FMCW) radar systems with different antenna arrays for the the purpose of three-dimensional target localization have been developed and studied over the years. A compact 16 GHz MIMO FMCW radar system with 16 TX and 16 RX antennas, forming a rectangular virtual array with 256 equally spaced elements, has been presented in [1, 2]. The system achieved an angular resolution of 4.7° in azimuth and 3.6° in elevation, respectively. This MIMO concept was extended to a modular 24×24 channel system with a resolution of 2.9° [3]. Another 24×24 MIMO FMCW radar system operating at 120 GHz was developed in [4]. By using a sparse antenna array with a semi-circular arrangement for the TX and RX antennas, an angular resolution of about 1° for both azimuth and elevation was achieved.

For a MIMO radar system with a given number of TX and RX channels, the highest angular resolution is achieved when the virtual array is linear, with all antenna elements distributed along a common axis. A 77 GHz MIMO FMCW radar with this type of antenna arrangement was shown in [5]. By use of six TX and eight RX antennas, a linear virtual array of 48 equally spaced elements was formed, and an angular resolution of 3° was achieved. However, there is a limitation due to the linear antenna arrangement. Depending on the system's orientation, either the azimuth or the elevation angle of a target can be determined, but not both at the same time. Therefore, only the two-dimensional position of a target (R, ϕ) can be estimated. This limitation was removed by a concept presented in [6], where a 77 GHz MIMO FMCW radar with a linear array was equipped with frequency-steered TX antennas. Even though the system had a linear virtual array, this approach enabled a three-dimensional target localization (R, ϕ, θ). The system benefits from a high resolution in azimuth and an additional resolution in elevation at the cost of range resolution.

The frequency-controlled antennas we use in our system are of the slotted waveguide antenna type. The concept of a small slot array, first described in [7], was adapted to substrate integrated waveguide (SIW) technology in [8, 9], enabling its use in millimeter wave applications. A particular form of this antenna was later introduced in [10], in which a meander shape
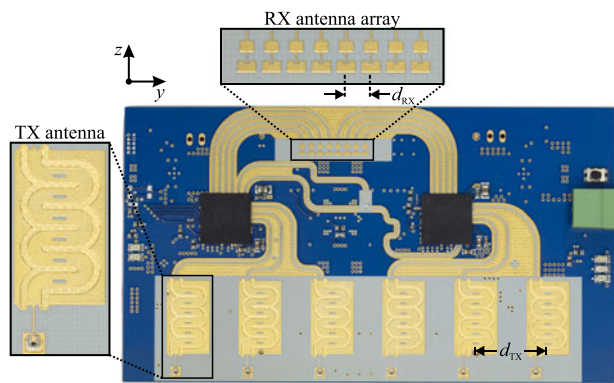
Figure 1. MIMO FMCW radar system with master and slave transceiver ICs. The eight RX antennas are arranged in $\lambda_c/2$ spacing, and the six frequency-steered TX antennas in $8\lambda_c/2$ spacing. The multilayer board with a core stackup of $1 \times RO4350B + 4 \times FR4$ is of size $100 \times 60\ \text{mm}^2$.

Figure 2. Sketch of the TX and RX antenna patterns when considering the system in a side view. The RX antennas have a wide beam that remains rather constant throughout the frequency chirp. The main lobe of the TX antennas is continuously tilted downward during the chirp. A target is detected during a certain part of the frequency ramp. The information about the target angle is contained in the amplitude of the intermediate frequency signal.

increased the electrical length between two adjacent slots. Thereby, frequency-dependent phase differences arise between the slots, enabling a frequency-dependent control of the main lobe. Due to its high bandwidth, this antenna is ideally suited for millimeter wave FMCW radar systems that generate linear frequency chirps. For example, a system for tracking very fast objects [11–13] and an imaging radar [14] have been developed based on this antenna.

The capabilities of a MIMO radar with frequency-steered antennas based on the concept in [6] have already been demonstrated by measurements using a vector network analyzer and mechanically moved antennas in [15]. In this contribution, we present a corresponding standalone system that is characterized by measurements. The focus is on estimating range and angular resolution in both azimuth and elevation and on the three-dimensional target localization. An earlier version of this paper was presented at the 19th European Radar Conference and was published in its proceedings [16].

System design

Radar hardware

Our developed radar system, shown in Fig. 1, comprises two AWR1243P automotive radar ICs from Texas Instruments that generate FMCW chirps in a frequency range of 77–81 GHz. To ensure coherent signal generation, these ICs are arranged in a cascaded mode. One IC functions as the master, supplying a 20 GHz reference signal. This reference signal is split by a Wilkinson divider located at the board's center and then fed back to each device, where it is used as the reference for chirp generation. The same feedback mechanism is employed for a digital trigger signal to enable synchronous sampling. Each of the RX channels on the ICs is equipped with an integrated analog-to-digital converter (ADC), capable of generating complex 12-bit samples with a maximum sampling rate of 18.75 Msps. However, a 10 Msps sampling rate is used for the measurements in "Measurement" section. The ADC data is transmitted through a low voltage differential signaling interface on the backside of the board to a MicroZed platform from Xilinx, where the data is stored and processed. Each AWR1243P device contributes three TX and four RX channels, resulting in a total of six TX and eight RX channels. The system operates in a time-division multiplexing mode, with the six TX channels sequentially transmitting chirps.
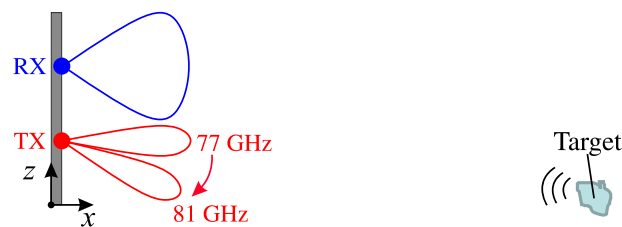
Antenna distribution and characteristics

The spatial distribution of the antennas interconnected to the TX and RX channels through grounded coplanar waveguides is shown in Fig. 1. Both the TX and RX arrays are arranged in a linear fashion, with a TX spacing of $d_{\text{TX}} = 8\,d_{\text{RX}}$ and an RX spacing of $d_{\text{RX}} = \frac{\lambda_c}{2}$, where λ_c is the free space wavelength at the center frequency $f_c = 79\,\text{GHz}$. This configuration results in a linear virtual array consisting of 48 channels, as was also realized in [5].

As outlined in "Introduction" section, our system's concept is based on a frequency-dependent combined antenna pattern of the virtual channels. For a given virtual channel consisting of a TX–RX pair, the corresponding combined antenna pattern can be obtained by multiplying the individual TX and RX patterns, schematically illustrated in Fig. 2. While the RX antennas exhibit a wide beam, the TX antennas are engineered to focus within the elevation plane. The main lobe of the TX antennas is steerable and adjusted according to the chirp's frequency. When operating at 77 GHz, the beam aligns perpendicularly to the board's surface, continuously tilting downwards as the frequency increases during the chirp.

The TX antennas were designed according to the principle described in [10]. In this process, slots are inserted into a meandered SIW at defined intervals, as shown in Fig. 3. Each TX antenna comprises a linear array composed of six series-fed slots that collectively generate a fan beam in the far-field region, focused in the elevation plane. The extension in azimuth of this fan beam is particularly advantageous for the MIMO system's field of view. The transmit signal is fed into the antenna's input port, traversing the meander-shaped SIW structure. At the output, the signal is transferred to a microstrip line through a tapered transition and finally terminated by a chip resistor. At each slot, a portion of the signal's power is radiated into free space. The relative phase difference $\Delta\varphi_s$ depends on the length L_s of the SIW sections between adjacent slots and the guided wavelength or frequency. In our design, we choose L_s to equal twice the guided wavelength at 77 GHz, corresponding to a phase shift of $2 \cdot 360 = 720$ degrees. Since all slots radiate in phase ($\Delta\varphi_s = 0$), the main lobe is aligned perpendicular to the board's surface at 77 GHz. Deviations from 77 GHz cause progressive phase distributions along the slots ($\Delta\varphi_s \neq 0$), leading to a downward tilt of the main lobe. The total scanning angle depends on the bandwidth, the length L_s, and the phase constant of the SIW.

For the RX channels, double patch antennas (see Fig. 1) with a slightly focused beam in the elevation plane are used. Since the patches are fed serially, their main lobe direction also varies with frequency. This effect, however, is small due to the short electrical length between the patches. The patch antennas feature a substantially wider elevation beam compared to the slot
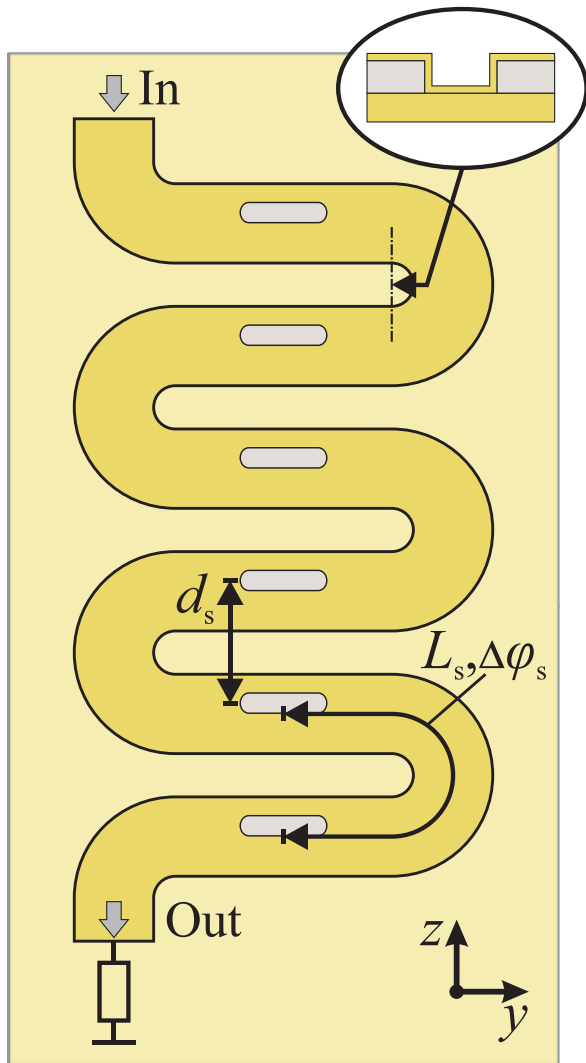
Figure 3. Schematic of the frequency-steered TX antenna. The wave propagates through the meandered SIW structure, with a portion of its power radiated into free space at each slot. The slots form a linear antenna array. Due to the large electrical length of the SIW, there are frequency-dependent phase settings at the slot positions which determine the direction of the main lobe.

antenna array. As a result, the combined pattern, notably the dependence of the main lobe direction on frequency, is primarily determined by the TX antennas.

Measurement

This section presents the measurements conducted for the system's characterization. Specifically, we aim to determine the separability of targets across all dimensions: ΔR, $\Delta \phi$ and $\Delta \theta$. Throughout these measurements, one or two test targets, namely corner reflectors, were strategically positioned at various locations within the far-field region of the sensor. The measurement setups, including the target arrangements for measurements labeled a-d, are depicted in Fig. 4. All measurements were performed within an anechoic chamber, ensuring controlled testing conditions. The corner reflectors were manually positioned and aligned using tape measures and floor markings. Hence, the target positions may exhibit slight deviations from their defined values. The objective of measurement

"Combined TX–RX antenna pattern" (a) is to derive a combined antenna pattern for each of the TX–RX pairs, depending on elevation angle and frequency. The derived pattern serves as a reference for determining the elevation angle in the subsequent measurements. In measurement "Target separability: azimuth plane" (b), two targets are positioned side by side at the same height, and their separability in the azimuth plane is examined. This is followed by measurement "Target separability: elevation plane" (c), where one target is positioned below the other, and the height of the lower target is varied. Finally, measurement "Three-dimensional target position" (d) serves to demonstrate the complete functionality of the system. In this case, two targets are positioned side by side, but at different heights, enabling us to exemplify the determination of their three-dimensional positions.

Combined TX–RX antenna pattern

The system's capability to detect targets in the elevation plane depends on the combined antenna patterns of the virtual antenna elements, each corresponding to a specific combination of TX and RX channels. To ascertain these patterns, the system is affixed to a tripod and positioned on a turntable, which is actuated by a stepper motor, allowing for the adjustment of the angle between the system and the target. A single corner reflector serves as a point-like target and is situated at a distance of 3 m in a direct line of sight. Both the system and the target are positioned at an approximate height of 1.5 m above the ground. For this particular measurement, the system is aligned, as depicted in Fig. 4a, with the virtual array axis pointing upwards. Therefore, contrary to the system's intended use case, the beam steering by frequency occurs in the azimuth plane and not in the elevation plane. Since it is actually the elevation angle that is altered by the stepper motor, it is also denoted as θ in this measurement. The angle θ is varied from $-90°$ to $90°$ in $2°$ increments. At each angular increment, a measurement is conducted using a frequency chirp spanning 77–81 GHz.

In the following, we derive the frequency-dependent patterns from the measurement data by performing the signal processing sequence, illustrated in Fig. 5, separately for each virtual channel.

Step I

The IF signal consists of $N = 1024$ samples ($n = 0, \dots, 1023$). Since the frequency of the transmitted chirp linearly depends on the sampling time, the instantaneous chirp frequency $f_{RF,n}$ can be assigned to each sample, with n denoting the corresponding sample index. An axis for $f_{RF,n}$ is added in Fig. 5, with values ranging from $f_{min} = 77.2$ GHz for the first sample to $f_{max} = 80.8$ GHz for the last sample. A 200 MHz offset from the start and end of the frequency ramp was chosen to mitigate transient effects, albeit at the expense of a reduced effective bandwidth of $B_{eff} = 3.6$ GHz.

The IF signal is analyzed using a sliding window FFT algorithm. A window of defined width w is slid over the signal sample by sample ($\Delta n = 1$). At the initial window position the left window limit coincides with the first sample ($n = 0$), and at the final window position, the right window limit coincides with the last sample ($n = 1023$). At each step, the samples within the window are extracted for separate processing in step II. For this and all subsequent signal processing steps where the sliding window algorithm is applied, the window width is consistently set to $w = 128$. This results in $N - w + 1 = 897$ window positions, dividing the complete IF signal into 897 separate sub-signals. Each sub-signal represents a specific frequency region of the chirp and is assigned to the center frequency of the corresponding window, denoted as $f_{w,n}$.
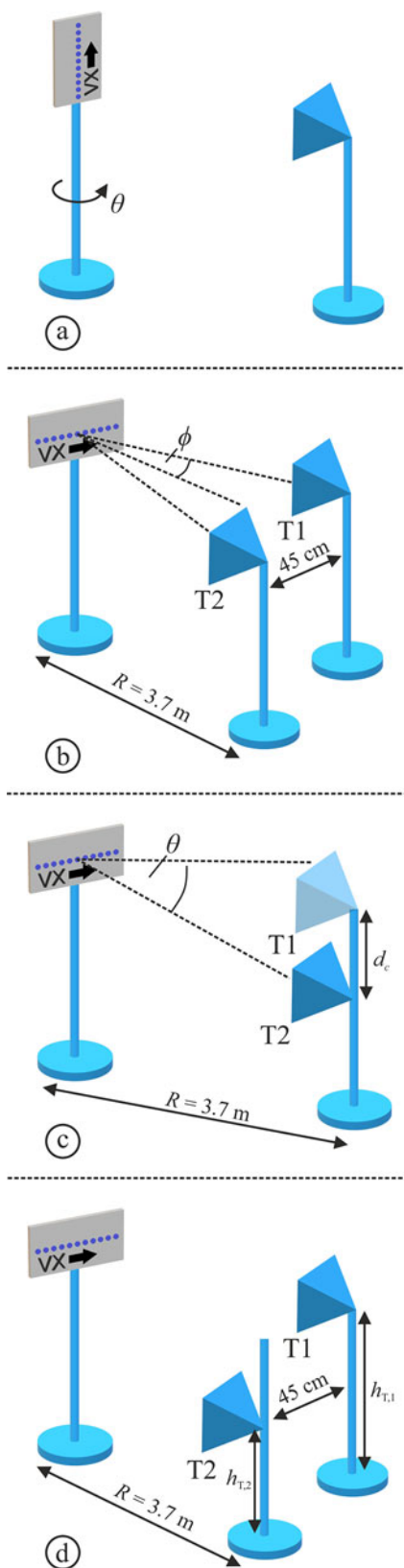
Figure 4. Positioning of the corner reflectors for measurements a–d. The direction of the virtual array axis VX is indicated with a bold arrow in each case.

For example, at the first position the window's center is located at sample $n = w/2 = 64$, with the corresponding window frequency being $f_{start} = f_{w,0} = f_{RF,64} = 77.5$ GHz.
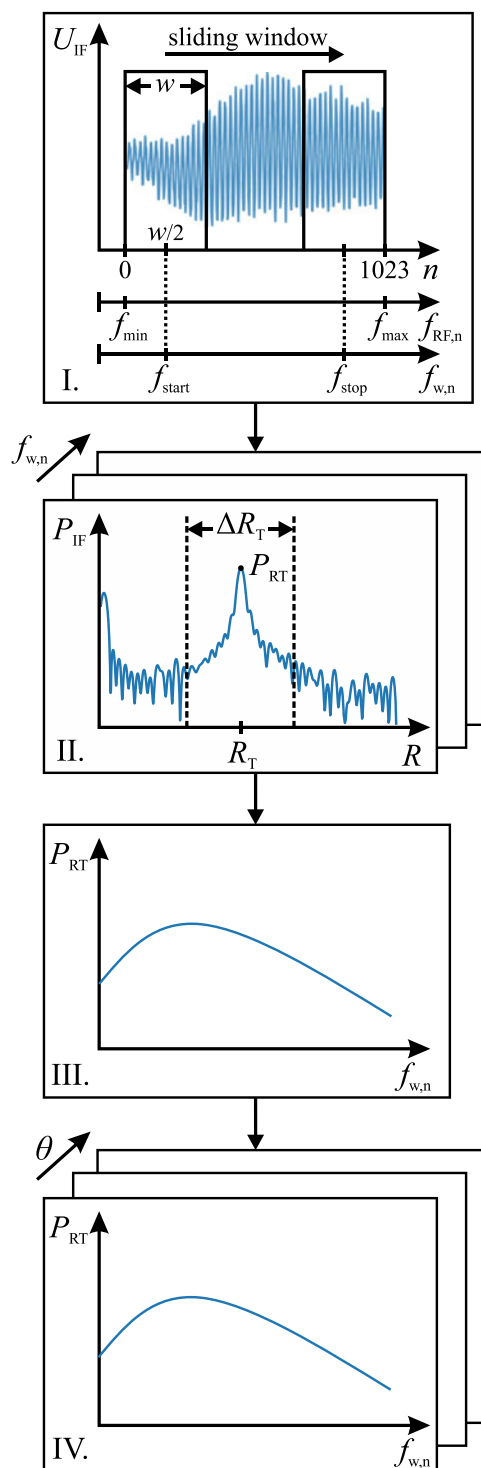

Figure 5. Signal processing sequence for generation of a single combined TX–RX antenna pattern. I: A window with a defined width w and center frequency $f_{w,n}$ is moved over the intermediate frequency (IF) signal sample by sample. II: At each position of $f_{w,n}$, a range fast Fourier transform (FFT) is performed and the magnitude P_{RT} of the target peak is determined. III: P_{RT} is plotted against $f_{w,n}$. IV: Steps I–III are repeated for all angular increments of the stepper motor.

Step II

For each of the 897 sub-signals obtained from step I, a range FFT is performed. According to the expectation, a single target becomes visible. The sliding window with $w = 128$ covers one-eighth of
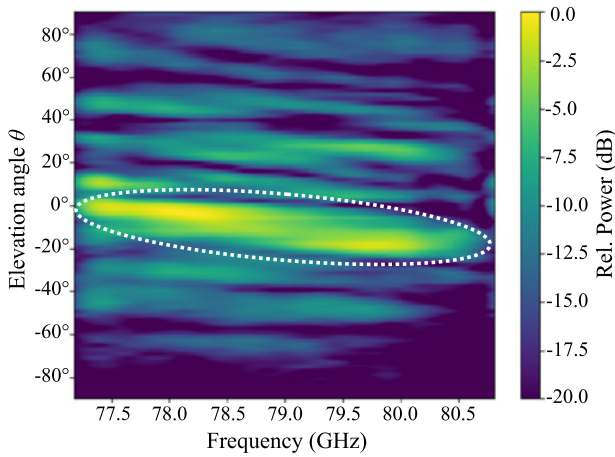
Figure 6. Measured combined antenna pattern in elevation plane for summed virtual channels corresponding to TX3 for azimuth angle $\phi = 0°$ (Fig. 4a). The main lobe direction changes with frequency, covering an angular range of approximately 20°.
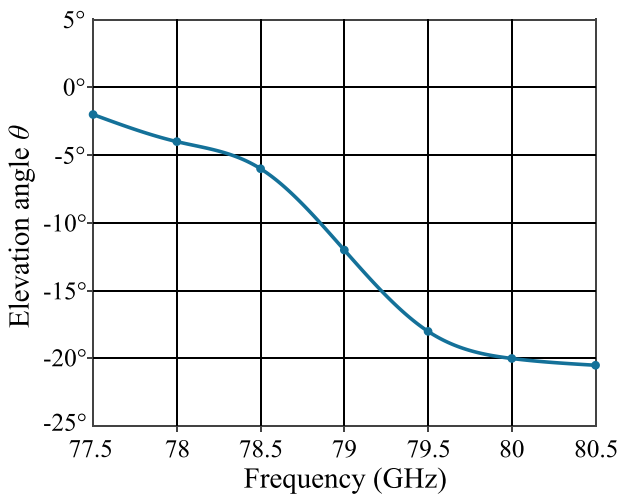

Figure 7. Main lobe direction of the combined pattern dependent on frequency, derived from Fig. 6. This figure serves as a frequency-dependent angular reference for determining θ.

the total frequency chirp, resulting in each sub-signal having an effective bandwidth of $B_{\text{eff,sub}} = \frac{1}{8}B_{\text{eff}} = 450\,\text{MHz}$. Due to the reduced bandwidth, the peak appears wider in range compared to the case where the FFT would have been performed on the entire IF signal. However, this is not an issue in this single-target environment. The chosen window width is a reasonable value in order to achieve sufficient frequency resolution while avoiding an excessive number of window steps, resulting in unnecessary computational overhead. For each computed range profile, the target's peak power P_{RT} is determined in a defined region ΔR_{T} around the known target position R_{T}.

Steps III and IV

The previously determined values for P_{RT} are plotted against their associated window frequencies $f_{\text{w,n}}$. The steps I to III are repeated for all angular increments of θ. The result of this processing is a data set containing the frequency-dependent amplitude response of a single virtual channel depending on θ. Finally, the signal processing sequence is performed for all virtual channels.

Based on the gained data set, the combined pattern is visualized as a color plot, where P_{RT} is normalized to its maximum value and plotted against frequency and θ, with the frequency directly corresponding to $f_{\text{w,n}}$. The summed-up pattern of the eight virtual channels belonging to TX3, which is located near the board's center, is shown in Fig. 6.

As can be seen, the main lobe of the combined pattern is tilted by about 20° in the considered frequency range. The extracted half-power beamwidth ranges between 5° and 10°. In order to extract the frequency-dependent main lobe direction from Fig. 6, the maximum along the θ-axis is determined in 500 MHz steps on the frequency axis and plotted accordingly in Fig. 7. This figure serves as a reference for translating the frequency into a corresponding elevation angle.

The curve exhibits different slopes in the frequency regions of 77.5–78.5, 78.5–79.5, and 79.5–80.5 GHz, indicating distinct tilt rates $\frac{\partial \theta}{\partial f}$ of the main lobe. The TX antenna itself is expected to demonstrate a linear relationship between the main lobe direction and frequency, as shown in [12]. However, Fig. 7 shows the combined main lobe direction, representing the composite effect of both the TX and RX antennas. As previously stated, the main lobe direction of the slightly focused RX antenna also exhibits frequency dependence, albeit to a considerably lesser extent compared to the TX antenna. As a result, the combined behavior exhibits variations regarding the tilt rate, depending on the instantaneous alignment of the TX and RX main lobe.

Target separability: azimuth plane

To determine angular and range resolution in the azimuth plane, the system is aligned, as shown in Fig. 4b, with the virtual array axis parallel to the ground. Two targets are placed adjacent to each other at a distance of 3.7 m, with a horizontal separation of 45 cm between them.

Each measurement involves raw data composed of 1024 complex samples for each virtual channel of the system, resulting in a two-dimensional matrix sized 48 × 1024, with virtual channels and IF samples as its dimensions. First, the inequalities of the virtual channels with respect to phase and amplitude are eliminated through a calibration following the procedure outlined in [17]. A correction matrix for phase and amplitude is derived from a measurement taken with a single corner reflector positioned in the far field region at $\phi = 0°$, $\theta = 0°$. Subsequently, each measurement data matrix is multiplied element-wise by this correction matrix.

From the calibrated raw data, a range-azimuth plot is generated using the signal processing steps depicted in the left column of Fig. 8. After applying Hann windows to both dimensions of the data matrix, an FFT is first performed along the virtual channel axis and then along the sample axis. The measurement result is visualized in Fig. 9, where the two targets, T1 and T2, are discernible, and their positions can be determined using a peak detection algorithm. For a more detailed analysis, a sectional view for $R = 3.7$ m is presented in Fig. 10. At this distance, the section plane passes exactly through the maximum of target T2. However, due to positioning inaccuracies, the maximum of T1 is slightly offset in range and not exactly situated on the section plane, resulting in the peak of T1 being approximately 6 dB lower than that of T2. Additionally, the targets are not symmetrically located around 0°. There is an offset of roughly 1.2° from the center, which can also be attributed to positioning inaccuracies.
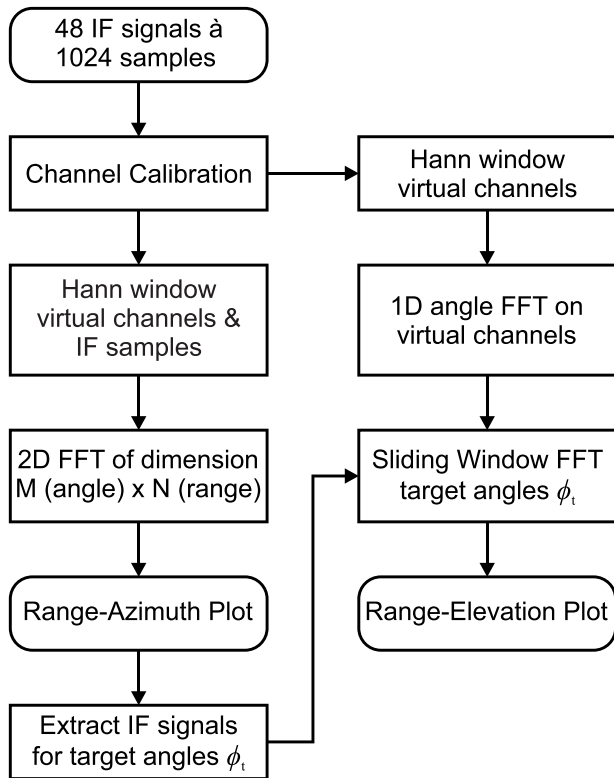
Figure 8. Signal processing steps for the generation of the range-azimuth and range-elevation color plots. The left column contains a direction of arrival algorithm, the right column a sliding window FFT algorithm.

Figure 9. Measurement of two corner reflectors symmetrically placed around $\phi = 0°$ in front of the system and located at the same height above the ground (Fig. 4b). The range-azimuth plot was generated by applying the signal processing steps in Fig. 8 (left column) and normalization to the maximum peak power. The targets, which are 45 cm apart, are identifiable by two distinct peaks.

Figure 10. Cross-sectional view derived from Fig. 9 at $R = 3.7$ m. The two targets are visible as two distinct peaks with a 3-dB width of 3.5°. Due to alignment inaccuracy, the peaks are shifted 1.2° off center.

Nevertheless, the two targets are clearly distinguishable from each other. The 3-dB width, which is a measure for the angular resolution, is $\Delta\phi_{3dB} = 3.5°$ for both target peaks. This implies that the azimuth resolution closely aligns with the results presented in [5] and could potentially be further improved by eliminating the Hann window, albeit at the expense of increased side lobes. In terms of range resolution, Fig. 9 reveals a value of $\Delta R = 9.0$ cm for both targets. The range resolution of the system is slightly lower than that of a conventional FMCW radar system with a range resolution of $\Delta R_c = w_{hann} \cdot \frac{c_0}{2B} = 7.5$ cm. Unlike in a conventional FMCW radar system, the total effective bandwidth is distributed over an angular range of θ. The target is present within the main lobe of a TX–RX pair only during a specific frequency range of the chirp. The bandwidth contained within this frequency range, which is crucial for range resolution, depends on two factors: the tilt rate $\frac{\partial\theta}{\partial f}$ and the angular extent of the combined main lobe. Since the main lobe is steered over a rather narrow angular range of approximately 20°, exhibiting a wide half-power beamwidth of up to 10°, the loss in resolution is only 1.5 cm or 20% when referenced to $\Delta R_c = 7.5$ cm.

Target separability: elevation plane

This measurement aims to investigate target separability in the elevation plane. The system is set up with the same orientation as for the azimuth measurement. However, the two targets are not placed next to each other, but one below the other, as illustrated in Fig. 4c. Measurements are conducted for the corner distances d_c ranging from 20 to 80 cm. The targets are located at a distance of 3.7 m, with the upper targ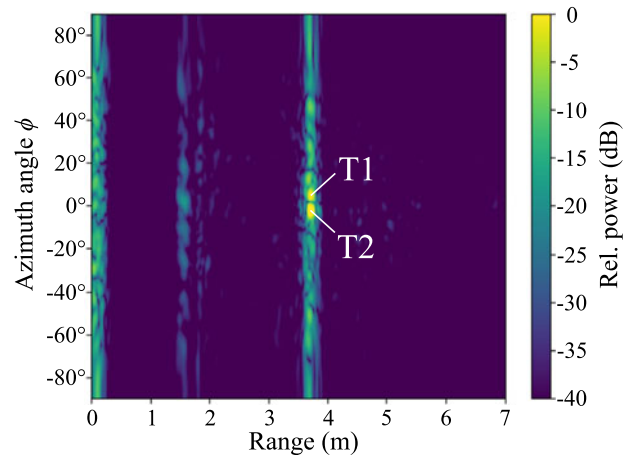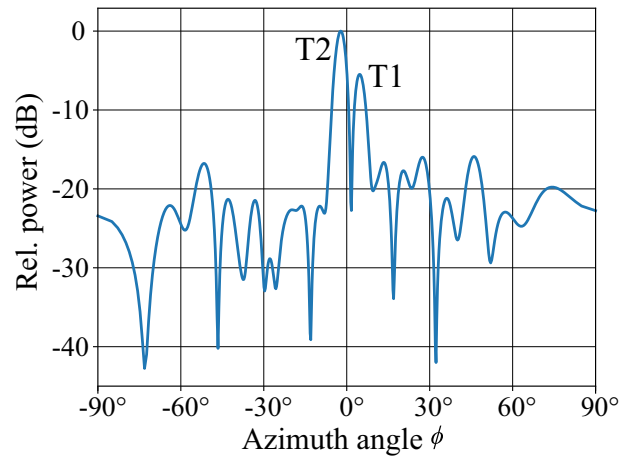et located approximately 6 cm below the center of the virtual array. During the measurement, the upper target is not moved and remains stationary. For comparison, measurements are then repeated with only one target, positioned at the same locations previously occupied by the lower target.

To generate the range-elevation plots from the measurement data, a sliding window FFT according to step I in Fig. 5 is applied to the IF signals of the virtual channels. As in measurement "Combined TX–RX antenna pattern", a window width of $w = 128$ samples was chosen, corresponding to a bandwidth of 450 MHz. At each window step $f_{w,n}$, the IF signal within the window, representing a specific frequency region of the chirp, is multiplied by a Hann window and subjected to an FFT. In this measurement, the choice of the window width is a trade-off between range and elevation resolution. A window width of 128 samples or 450 MHz places both quantities into a reasonable proportion. However, the range resolution for a given elevation angle is physically limited by the half-power beamwidth of the combined antenna pattern.

The resulting range-frequency plots for the performed measurements, depicting relative power as a function of frequency
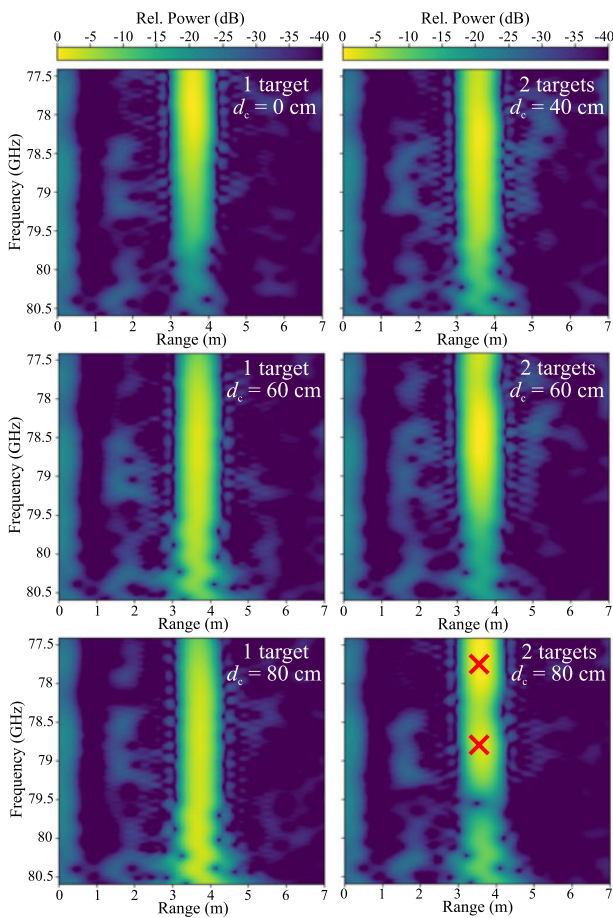
Figure 11. Measurement of a single target (left column) and two targets (right column) in the elevation plane (Fig. 4c). The range-frequency plots, normalized to the maximum, were generated using a sliding window FFT algorithm. As the distance d_c increases, the peak of the moved target shifts to higher frequencies (θ). The targets appear broadened in frequency, which is due to a rather small scanning angle in combination with a large half-power beamwidth of the combined antenna. In the plot in the bottom right corner, where two separate peaks become visible, the target positions are marked with red crosses.
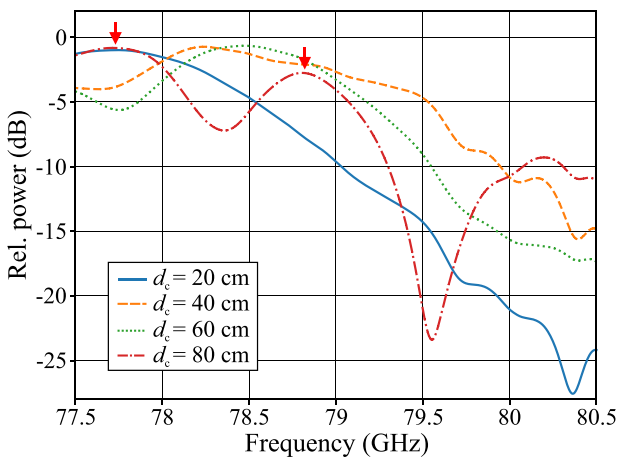

Figure 12. Cross-sectional view at $R = 3.7$ m, derived from Fig. 11 (right column). For distances d_c between 20 and 80 cm, the peaks of the targets merge into each other. Only at a distance of $d_c = 80$ cm the targets can be clearly separated from each other.

and range, are shown in Fig. 11. In the left column, the results of the single target environment are presented, while in the right column, the results of the double target environment are depicted. The frequency can be translated into a corresponding elevation angle using Fig. 7. The targets appear wide in elevation, primarily due to the wide main lobe of the combined pattern and the low tilt angle. However, for each height in the single target measurement, a distinct maximum can be identified. For a more detailed analysis of the double target measurement, the slices at $R = 3.7$ m are considered in Fig. 12. As can be seen, the two targets are only distinguishable at $d_c = 80$ cm. The peak of the lower target is located at $f_{T2} = 78.8$ GHz, corresponding to an elevation angle of about $\theta_{T2} = $-10°. The lower target has a 3-dB width of $\Delta f_{3dB} = 620$ MHz, which can be converted to an elevation angle width of $\Delta \theta_{3dB} = 7.8°$. It is noted that this result is dependent on the signal processing method previously described.

Three-dimensional target position

In this measurement, the two targets T1 and T2 are positioned adjacent to each other as in measurement "Target separability: azimuth plane". However, in this configuration, the targets also vary in height, as illustrated in Fig. 4d. Here, target T1 is located 30 cm below the center of the virtual array, while target T2 is situated 60 cm below T1.

To determine the three-dimensional coordinates (R, θ, ϕ) of the targets, all the signal processing steps outlined in Fig. 8 are applied. It is required to start with the left column to determine the azimuth angles ϕ_{T1} and ϕ_{T2} first. After calibration and applying a Hann window to the IF data, a two-dimensional FFT is performed along the virtual channels and the IF samples. The resulting plot is shown in figure Fig. 13a. As expected, two distinct target peaks are discernible near $\phi = 0°$. The center point between the targets deviates from 0° due to an alignment error of the measurement setup. The peak positions can be determined using a peak detection algorithm, leading to $\phi_{T1} = -0.3°$ and $\phi_{T2} = -7.1°$, and the corresponding range values $R_{T1} = 3.7$ m and $R_{T2} = 3.8$ m. When compared to the range-azimuth plot of measurement "Target separability: azimuth plane" (see Fig. 9), it is evident that the range value associated with T2 is approximately 10 cm greater than that of T1. This is plausible since T2 is located 60 cm below T1, and thus further away from the system.

For the complete three-dimensional position, the elevation angle θ remains to be determined. This is accomplished by applying the signal processing steps outlined in the right column of Fig. 8. After windowing and zero padding, a one-dimensional FFT is exclusively performed along the virtual channels. The outcome is an array in which the IF signals are arranged in ascending order versus the azimuth angle ϕ, as shown in Fig. 13b. Due to the zero padding, there are more IF signals than physical virtual channels after the FFT. These additional IF signals are artificially generated and do not increase the number of physical virtual channels. In Fig. 13b, the two targets appear as two separate lines located at the corresponding azimuth angles. Furthermore, both lines exhibit different amplitude signatures, which inherently encapsulate information about the elevation angle. From the data array in Fig. 13b, the IF signals at the previously determined target angles ϕ_{T1} and ϕ_{T2} are extracted, and the sliding window FFT is applied two both IF signals. The resulting range-frequency plots are shown in Fig. 14.
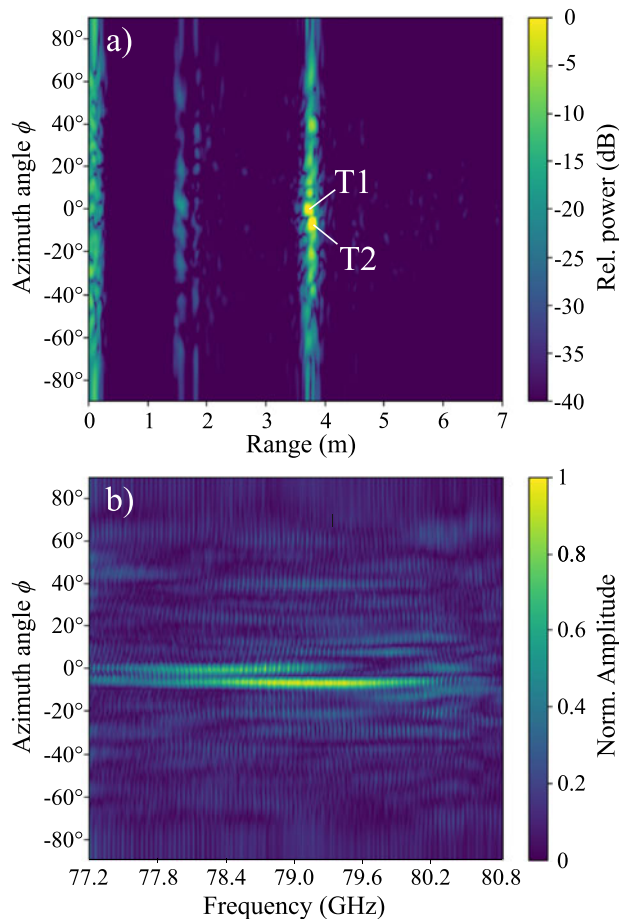
Figure 13. Measurement of two corner reflectors placed 45 cm apart from each other near $\phi = 0°$ and additionally positioned at different heights above the ground (Figure 4d). (a) The range-azimuth plot was obtained by applying the signal processing steps in Figure 8 (left column) and normalization to the maximum peak power. (b) The first two processing steps in the right column of Figure 8 were executed. In this process, an FFT was exclusively applied along the virtual channels, sorting the IF signals according to the azimuth angle. The sorted IF signals are then plotted against the chirp frequency and presented in a normalized plot. The targets appear as two separate lines with different amplitude profiles, which inherently contain information about the elevation angle.
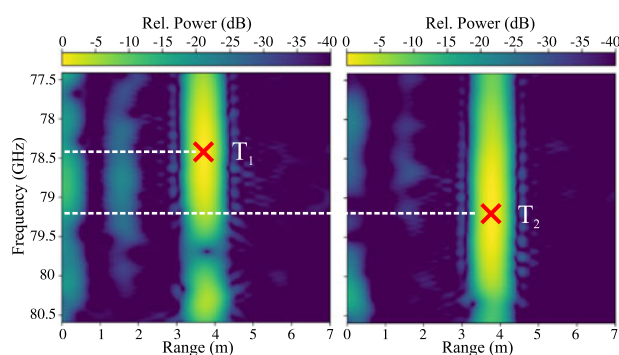

Figure 14. Range-frequency plots generated by applying a sliding window FFT to the two IF signals extracted from Fig. 13b at corresponding azimuth angles ϕ_{T1} and ϕ_{T2}. The target peaks are located at different frequencies, yielding the corresponding elevation angles θ_{T1} and θ_{T2} by translating with Fig. 7.

As expected, the target T2 is situated below T1. The corresponding target frequencies $f_{T1} = 78.4\,\text{GHz}$ and $f_{T2} = 79.2\,\text{GHz}$ are converted

into the respective elevation angles $\theta_{T1} = \text{-6°}$ and $\theta_{T2} = \text{-15}\,°$ using Fig. 7.

Conclusion

In this contribution, we presented a MIMO FMCW radar system featuring a linear virtual array configuration, equipped with frequency-steered antennas for the transmit channels and dual patch antennas for the receive channels. This TX–RX antenna combination effectively eliminated the spatial constraints associated with a linear array, enabling three-dimensional target localization. Our evaluation of the system's performance involved a comprehensive series of measurements, focusing on target separability and the determination of three-dimensional target positions. Measured by the 3-dB width of the target peaks, the system has a high azimuth resolution of $\Delta\phi_{3dB} = 3.5°$, a range resolution of $\Delta R = 9\,\text{cm}$ and an elevation resolution of $\Delta\theta_{3dB} = 7.8°$, taking into consideration the broadening effect introduced by a Hann window. When designing the system for real-world applications, these resolutions can be tailored by appropriately configuring the number of TX or RX channels, as well as adjusting the total scanning angle and the beamwidth of the frequency-steered transmit antennas.

To further enhance the system, frequency-steered antennas could be employed for both TX and RX. This approach would increase the directivity of the combined pattern and result in a significantly sharper frequency-dependent main lobe, thereby leading to improved elevation resolution. However, it is not feasible to directly replace the RX antennas with the TX antennas used for this system since they cannot be arranged in a $\lambda_c/2$ spacing due to their substantial dimensions. This would only be possible if a substrate with significantly higher permittivity were used, potentially eliminating the meander shape and connecting the slots with straight-line SIW sections. Nevertheless, this approach comes with considerably higher technical demands on the manufacturing process, particularly regarding via technology, as well as higher losses.

Competing interests.   None declared.

References

1. **Mietzner J, Lutz S, Weckerle C, Hofstaetter B, Miralles E, Ganis A, Multerer T, Puchinger J, Prechtel U, Ziegler V and Meusling A** (2017) Compact 3D MIMO radar – antenna array design and experimental results. In *2017 European Radar Conference (EURAD)*, Nuremberg, Germany. New York: IEEE, 130–133.
2. **Miralles E, Multerer T, Ganis A, Schoenlinner B, Prechtel U, Meusling A, Mietzner J, Weckerle C, Esteban H, Vossiek M, Loghik M and Ziegler V** (2018) Multifunctional and compact 3D FMCW MIMO radar system with rectangular array for medium-range applications. *IEEE Aerospace and Electronic Systems Magazine* **33**(4), 46–54.
3. **Ganis A, Miralles E, Schoenlinner B, Prechtel U, Meusling A, Heller C, Spreng T, Mietzner J, Krimmer C, Haeberle B, Lutz S, Loghi M, Belenguer A, Esteban H and Ziegler V** (2018) A portable 3-D imaging FMCW MIMO radar demonstrator with a 24 × 24 antenna array for medium-range applications. *IEEE Transactions on Geoscience and Remote Sensing* **56**(1), 298–312.
4. **Kueppers S, Cetinkaya H, Herschel R and Pohl N** (2020) A compact 24 × 24 channel MIMO FMCW radar system using a substrate integrated waveguide-based reference distribution backplane. *IEEE Transactions on Microwave Theory and Techniques* **68**(6), 2124–2133.
5. **feger R, Pfeffer C and Stelzer A** (2014) A frequency-division MIMO FMCW radar system based on delta–sigma modulated transmitters. *IEEE Transactions on Microwave Theory and Techniques* **62**(12), 3572–3581.

6. **Orth A, Kwiatkowski P and Pohl N** (2019) A novel approach for a MIMO FMCW radar system with frequency steered antennas for 3D target localization. In *2019 16th European Radar Conference (EuRAD)*, Paris, France. New York: IEEE, 37–40.

7. **Elliott R and Kurtz L** (1978) The design of small slot arrays. *IEEE Transactions on Antennas and Propagation* **26**(2), 214–219.

8. **Yan L, Hong W, Hua G, Chen J, Wu K and Cui TJ** (2004) Simulation and experiment on SIW slot array antennas. *IEEE Microwave and Wireless Components Letters* **14**(9), 446–448.

9. **Xu F, Wu K and Zhang X** (2010) Periodic leaky-wave antenna for millimeter wave applications based on substrate integrated waveguide. *IEEE Transactions on Antennas and Propagation* **58**(2), 340–347.

10. **Shoykhetbrod A, Nussler D and Hommes A** (2012) Design of a SIW meander antenna for 60 GHz applications. In *2012 The 7th German Microwave Conference*, Ilmenau, Germany. New York: IEEE, 1–3.

11. **Hommes A, Shoykhetbrod A and Pohl N** (2014) A fast tracking 60 GHz Radar using a frequency scanning antenna. In *2014 39th International Conference on Infrared, Millimeter, and Terahertz waves (IRMMW-THz)*, Tucson, AZ, USA. New York: IEEE, 1–2.

12. **Shoykhetbrod A, Hommes A and Pohl N** (2014) A scanning FMCW-radar system for the detection of fast moving objects. In *2014 International Radar Conference*, Lille, France. New York: IEEE, 1–5.

13. **Shoykhetbrod A, Geibig T, Hommes A, Herschel R and Pohl N** (2016) Concept for a fast tracking 60 GHz 3D-radar using frequency scanning antennas. In *2016 41st International Conference on Infrared, Millimeter, and Terahertz waves (IRMMW-THz)*. Copenhagen, Denmark New York: IEEE, 1–3.

14. **Geibig T, Shoykhetbrod A, Hommes A, Herschel R and Pohl N** (2016) Compact 3D imaging radar based on FMCW driven frequency-scanning antennas. In *2016 IEEE Radar Conference (RadarConf)*, Philadelphia, PA, USA. New York: IEEE, 1–5.

15. **Shoykhetbrod A, Cetinkaya H and Nowok S** (2020) Measurement-based performance investigation of a hybrid MIMO-frequency scanning radar. In *2020 IEEE/MTT-S International Microwave Symposium (IMS)*, Los Angeles, CA, USA. New York: IEEE, 1251–1254.

16. **Kwiatkowski P, Orth A, Piotrowsky L and Pohl N** (2022) A 77-81 GHz FMCW MIMO radar with linear virtual array enabling 3D target localization by use of frequency-steered TX antennas. In *2022 19th European Radar Conference (EuRAD)*, Milan, Italy. New York: IEEE, 221–224.

17. **Vasanelli C, Roos F, Durr A, Schlichenmaier J, Hugler P, Meinecke B, Steiner M and Waldschmidt C** (2020) Calibration and direction-of-arrival estimation of millimeter-wave radars: A practical introduction. *IEEE Antennas and Propagation Magazine* **62**(6), 34–45.

Patrick Kwiatkowski (Graduate Student Member, IEEE) received the B.Sc. and M.Sc. degrees in electrical engineering and information technology from Ruhr University Bochum, Germany, in 2015 and 2020, respectively. He is currently pursuing the Ph.D. degree at the Institute of Integrated Systems, Ruhr University Bochum. His current research activities are in the field of novel multiple-input–multiple-output (MIMO) frequency-modulated continuous wave (FMCW) radar front-end concepts with a focus on antenna design.

Alexander Orth received the B.Sc. and M.Sc. degrees in electrical engineering and information technology from Ruhr University Bochum, Bochum, Germany, in 2014 and 2016, respectively. He is currently pursuing the Ph.D. degree at the Institute of Integrated Systems, Ruhr University Bochum. His current research activities are in the field of radar system design and radar signal processing for wearable radar systems in medical applications.

Nils Pohl (Senior Member, IEEE) received the Dipl.-Ing. and Dr.Ing. degrees in electrical engineering from Ruhr University Bochum, Bochum, Germany, in 2005 and 2010, respectively. From 2006 to 2011, he was a Research Assistant with Ruhr University Bochum, where he was involved in integrated circuits for millimeter-wave (mm-wave) radar applications. In 2011, he became an Assistant Professor with Ruhr University Bochum. In 2013, he became the Head of the Department of mm-wave Radar and High Frequency Sensors with the Fraunhofer FHR, Wachtberg, Germany. In 2016, he became a Full Professor for Integrated Systems with Ruhr University Bochum. In parallel, he is head of the Research group for Integrated Radar Sensors at Fraunhofer FHR. He has authored or coauthored more than 200 scientific papers and has issued several patents. His current research interests include ultra-wideband mm-wave radar, design, and optimization of mm-wave integrated SiGe circuits and system concepts with frequencies up to 500 GHz and above, as well as frequency synthesis and antennas. Prof. Pohl is a member of IEEE, VDE, ITG, EUMA, and URSI. He was a co-recipient of the 2009 EEEfCom Innovation Award, and a recipient of the Karl-Arnold Award of the North Rhine-Westphalian Academy of Sciences, Humanities and the Arts in 2013 and the IEEE MTT Outstanding Young Engineer Award in 2018. Additionally, he was co-recipient of the best paper award at EUMIC 2012, best demo award at RWW 2015, and best student paper awards at RadarConf 2020, RWW 2021 and EUMIC 2021.